

# Fast determination of cell anisotropy and size in epithelial tissue images using Fourier Transform

M. Durande (✉),<sup>1,2</sup> S. Tlili,<sup>1,3</sup> T. Homan,<sup>2</sup> B. Guirao,<sup>4</sup> F. Graner (✉),<sup>1</sup> and H. Delanoë-Ayari (✉)<sup>2</sup>

<sup>1</sup>*Laboratoire Matière et Systèmes Complexes, Université Denis Diderot - Paris 7,  
CNRS UMR 7057, 10 rue Alice Domon et Léonie Duquet, F-75205 Paris Cedex 13, France*

<sup>2</sup>*Univ. Lyon, Université Claude Bernard Lyon 1, CNRS UMR 5306,  
Institut Lumière Matière, Campus LyonTech - La Doua,  
Kastler building, 10 rue Ada Byron, F-69622 Villeurbanne Cedex, France*

<sup>3</sup>*Mechanobiology Institute, Department of Biological Sciences,  
National University of Singapore, 5A Engineering Drive, 1, 117411 Singapore*

<sup>4</sup>*Polarity, Division and Morphogenesis Team, Institut Curie, CNRS UMR 3215,  
INSERM U934, 26 rue d'Ulm, 75248 Paris Cedex 05, France*

Mechanical strain and stress play a major role in biological processes such as wound healing or morphogenesis. To assess this role quantitatively, fixed or live images of tissues are acquired at a cellular precision in large fields of views. To exploit these data, large number of cells have to be analyzed to extract cell shape anisotropy and cell size. Most frequently, this is performed through detailed individual cell contour determination, using so-called segmentation computer programs, complemented if necessary by manual detection and error corrections. However, a less detailed and faster technique can be recommended in at least three situations. First, when detailed information on individual cell contours is not required, for instance in studies which require only coarse-grained average information on cell anisotropy. Second, as an exploratory step to determine whether full segmentation can be potentially useful. Third, when segmentation is too difficult, for instance due to poor image quality or a too large cell number. We developed a user-friendly, Fourier Transform based image analysis pipeline. It is fast (typically  $10^4$  cells per minute with a current laptop computer) and suitable for time, space or ensemble averages. We validate it on one set of artificial images and on two sets of fully segmented images, from *Drosophila* pupa and chicken embryo; the pipeline results are robust. Perspectives include *in vitro* tissues, non-biological cellular patterns such as foams, and 3D images.

## I. INTRODUCTION

During important physiological processes such as wound healing, morphogenesis or metastasis, cells deform, migrate, exchange neighbors, divide and die. A proper mechanical description of such complex active system requires the characterization of cell size, cell shape and changes thereof [1]. Fluorescent labeling of cell contours and progresses in microscopy have led to the acquisition of large tissue images with high signal-to-noise ratio. Determination of individual cell contours have allowed to apply mechanical approaches based on quantitative data analysis of cell packing within epithelial tissues [2–4]; then to develop quantitative modeling of tissue structure [5–7]; and even link cell-level changes to morphogenetic movements [8–11]. While these studies were bidimensional, three dimensional studies are becoming increasingly current [12–14].

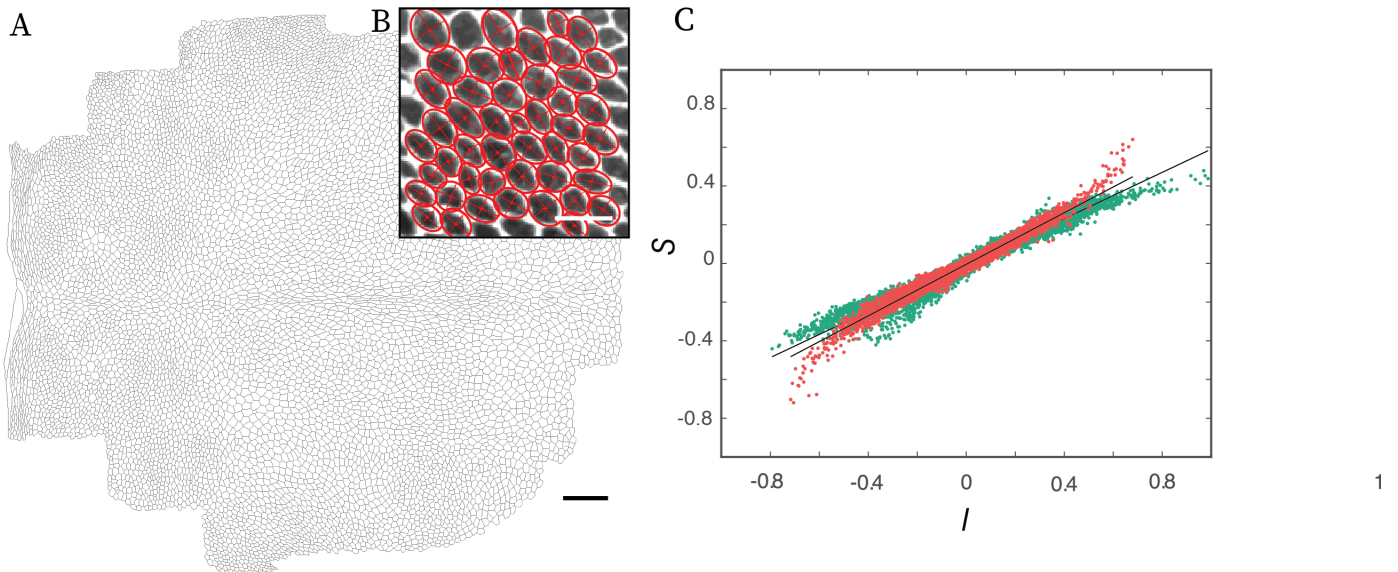


FIG. 1. Cell segmentation evidences a correlation between cell shape and elastic stress anisotropies. (A) Whole image segmented of the *Drosophila* dorsal thorax during its metamorphosis. Head is on the right of the image and abdomen on the left. Scale bar is  $50 \mu\text{m}$ . (B) Sub-image in original grey levels, scale bar is  $10 \mu\text{m}$ . Cells are transfected to label the membrane with a fluorescent marker (green fluorescent protein, GFP), imaged using an inverted confocal spinning disk microscope, and segmented using a home-made software followed by automatic and manual rounds of correction [10]. In B, the inertia matrix of each cell is superimposed as an ellipse. (C) Diagonal component (green) and off-diagonal component (red) of the cell-cell junction tension contribution to stress  $S$ , representing elastic stress anisotropy, versus the corresponding anisotropic (diagonal and off-diagonal) component of the inertia matrix  $I$ , representing cell shape anisotropy. Correlations coefficients are respectively 0.97 and 0.96, slopes are respectively 0.6, 0.67. Tensors built with data from [10], here plotted after adimensionalisation by the isotropic part of the respective tensor. To compute each of the 14112 points, tensors of individual cells are computed before being averaged in Eulerian grids of  $40 \times 40 \mu\text{m}^2$  with 50% overlap. Then a sliding average is performed on 2 h (24 frames) of time with a one hour overlap. Boxes at the pattern boundary which are filled at less than 30% by cells are excluded from the fit.

These studies have been performed successfully using detailed determination of cell contours, also called “cell segmentation”, either manual, automatic or a combination of both. Segmentation programs are available in an increasing number (see [11, 12, 15] and references therein). Fig. 1 presents an example of such segmentation, in which the dorsal thorax of a fruit fly (*Drosophila*) is imaged at the stage of pupa, i.e. during its metamorphosis from larva to adult. For each cell, the inertia matrix (see Appendix A) is computed and represented as an ellipse which fits the cell contour. It is completely defined by three parameters: its major and minor axis length ( $L_{maj}$ ,  $L_{min}$ ) and the orientation  $\theta$  of its major axis with respect to the  $x$ -axis. The inertia matrix can be averaged on any given region, yielding an average inertia matrix and thus an ellipse characterising the average cell size and shape in this region. The cell area is characterised by  $\pi L_{maj} L_{min}$ .

The ratio  $L_{maj}/L_{min}$  and the angle  $\theta$  characterize the anisotropic part of the cell shape and are expressed by the anisotropic part of the inertia matrix. Interestingly, it is shown with image analysis using force inference on detailed cell contours [10] that the anisotropic part of the inertia matrix correlates strongly with the anisotropic part of the stress at cell-cell junctions (Fig. 1C). This last result is in agreement with a recent theoretical prediction [16] (under the assumption that cell-cell junctions and sizes are homogeneous in the tissue) and suggests that at least in the

*Drosophila thorax* tissue, shape measurements could be used as a proxy to estimate stress. Moreover, the inertia matrix also correlates strongly with the texture tensor (See Appendix A, Fig. 9) that is used to define the statistical internal strain [17]. This reinforces the interest of cell shape measurements, as an approximative but fast and simple alternative to stress measurements. Since stress is defined as a coarse grained quantity over a tissue region, average shape measurements should suffice without need for detailed individual cell shape segmentation.

There are other cases where a segmentation-free method of cell shape determination is potentially useful. For instance, a fast exploration of cell shape variation in time and space could help determine its role in a given biological question, before undertaking the detailed segmentation. Or, it could partially replace segmentation in cases where the image quality makes it difficult to segment it with reasonable effort and sufficient precision: low or variable contrast, low signal to noise ratio, interrupted cell edges, large variability of cell sizes, variety of cell types or very contorted cell shapes. Even when the image can be segmented, the cell number can be way too large to enable segmentation within a reasonable amount of time.

Different techniques have been probed to quantify a pattern anisotropy without segmentation, such as Hough transform [18], Radon transform [19] or Leray transform [20]. Fourier, Hilbert, and wavelet analysis are common in image analysis, with comparable performances when tested on common benchmarks [21, 22]. Fourier transform (Fig. 2) has already been used to determine the anisotropy of intra-cellular myosin distribution [23]. One of the advantages of Fourier transform, beyond its simplicity, is that its amplitude (as opposed to its phase) is insensitive to small displacements of images; hence the Fourier amplitude measured on successive images, images from different regions, or images from different experiments can be averaged [23].

Here, we implement a Fourier transform based pipeline for coarse grained determination of the cell shape anisotropy in subregions of the whole image, resulting in cell shape anisotropy and orientation maps. Whenever possible, we determine the cell size too. We validate the pipeline with two already segmented images, in *Drosophila pupa* and in chicken embryo, and discuss its advantages. In a companion paper, we apply the pipeline to images where the cell contours are not contrasted enough to segment them.

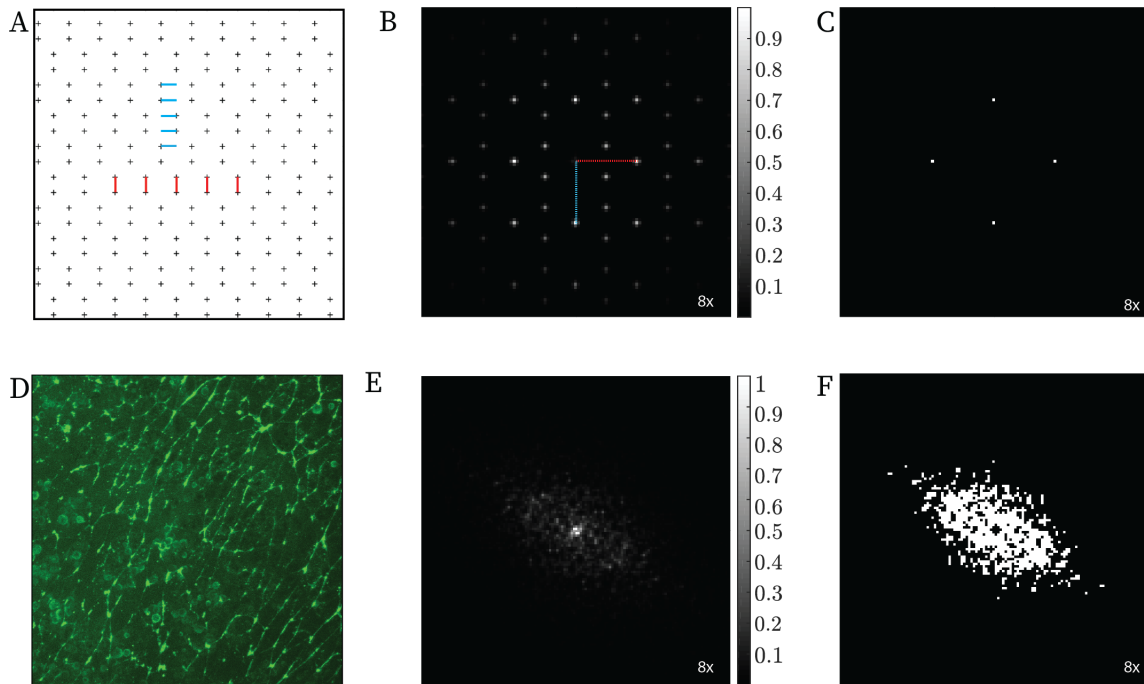


FIG. 2. Fourier Transform examples. (A) Points disposed in a periodic array. (B) Fourier spectrum of A with Gaussian blur of variance 0.6. (C) Same as B after selecting  $7 \cdot 10^{-4}\%$  of the points in the image within the brightest ones. The two principal directions are visible. (D) Anisotropic myosin distribution in the chicken embryo during morphogenesis, courtesy of K. Weijer. (E) Fourier spectrum of D with Gaussian blur of variance 0.6. (F) Same as E after selecting  $1 \times 10^{-1}\%$  of the points in the image within the brightest ones. The mention “8x” signifies that the spectra are zoomed 8 times.

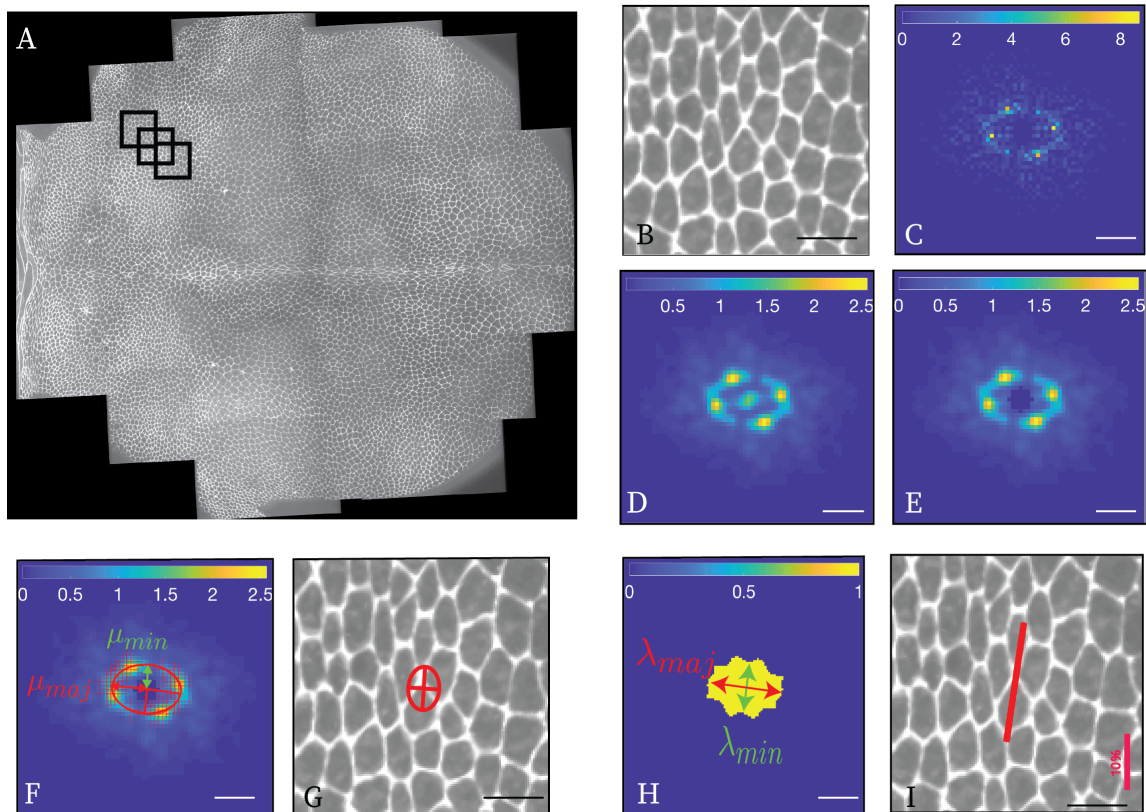


FIG. 3. Fourier Transform pipeline. (A) Whole segmented image in original grey levels, same data as Fig. 1A,B [10]. Boxes are examples of subwindows, showing their overlap. (B) Image in a subwindow, (C) its power spectrum density, (D) the power spectrum density after a Gaussian blur of variance 1.2. (E) After suppression of low frequencies (dark zone in the center). (F) An ellipse is fitted on the ring. Its axis orientations and lengths ( $\mu_{min}$ ,  $\mu_{maj}$ ) in the Fourier space define an ellipse with the same axis orientations and inverse axis lengths in the real space. (G) The ellipse size corresponds to the average cell size. (H) Filling the ellipse and measuring its FT inertia matrix improves the determination of pattern anisotropy, quantified by the ratio of ellipse axes  $\lambda_{min}/\lambda_{maj}$  in the Fourier space, and the direction  $\theta$  of the ellipse axes, but at the expense of absolute determination of axes sizes. Back in the real space (I), the pattern anisotropy is determined (its magnitude is represented by the bar size, and its direction is the direction of the bar) but not the cell area. For (C, D, E, F, H) scale bar is  $0.1 \mu\text{m}^{-1}$ . For (B, G, I) scale bar is  $10 \mu\text{m}$ , for (I) pink scale bar is 10 % of elongation.

## II. PIPELINE

The Fourier Transform (FT) of an ordered periodic pattern, such as a honeycomb, has peaks (Fig. 2A-C); the peak positions and intensities reveal the spatial periods and orientations present in the image. The FT of a disordered anisotropic pattern, such as the one computed on fibers, is a single broad distribution centered on zero frequency (Fig. 2D-F); the distribution width reveals the range of length scales present in the image, and the distribution anisotropy reveals the fiber anisotropy.

An epithelial tissue pattern (Fig. 3A) is aperiodic and usually lies in-between both extremes. The analysis is performed on overlapping subimages (Fig. 3A). The window size is chosen as a trade-off between the signal to noise ratio and the spatial resolution required to answer the question under consideration. Opposite borders in the image are not alike, but Fourier transform implicitly assumes that the image is periodic. This causes artifacts - such as a cross on the FT spectra - that is avoided by a periodic plus smooth image decomposition [24]. The FT phase provides information on the cell junction positions within each subimage, which is not of interest here. We keep only the FT amplitude. In Fourier space, we represent the FT power spectrum density, with the zero frequency at the center (Fig. 3C). We perform a time average over successive images; their number is chosen as a trade-off between the signal to noise ratio and time resolution required to answer the question under consideration. When the experiment is repeated, we average the FT spectrum of the different available samples (“ensemble average”); as opposed to space and time averages, ensemble averaging has only advantages in terms of signal to noise ratio.

The resulting power spectrum density is smoothed with a Gaussian blur (Fig. 3D). Low spatial frequencies, corresponding to lengthscales much larger than a cell size, are removed (Fig. 3E). The FT anisotropy reflects the pattern anisotropy; the FT itself is a blurred ring (Fig. 3C-E), more or less defined according to the initial image quality, and cell area variance. This enables two analysis possibilities of cell anisotropy: either with cell size (Fig. 3F,G) that we call the FT ellipse ring fit; or without it (Fig. 3H,I) that we call the FT inertia matrix. They are implemented as follows.

For a cellular pattern with a disorder in cell-cell junction orientation a small variance in area and a good image contrast, the FT is a well defined elliptic ring which can be fitted by an ellipse (Fig. 3F). Its axis sizes in Fourier space are  $(\mu_{maj}, \mu_{min})$ . They yield, back in real space, the ellipse axes sizes which describe the average cell properties within the subimage (Fig. 3,G):  $L_{maj} = \frac{2m}{\mu_{min}}$ ,  $L_{min} = \frac{2m}{\mu_{maj}}$ ; here  $m$  is the size of the FT image in pixels. To ensure the link with the real absolute size,  $L_{maj}, L_{min}$  have to be multiplied by the pixel size. The angle between the  $x$ -axis and major axis is  $\theta$  in real space and  $\theta + \pi/2$  in Fourier space.

The second method is less informative because it does not give access to the size, but more general for the definition of the anisotropy because it applies even if the FT ellipse ring is not well defined (as in Fig. 2). It uses the inertia matrix of a pattern (see Appendix A) to define a plain ellipse with a correct aspect ratio. From Fig. 3E the spectrum is binarized keeping a given percentile of the brightest pixels. A morphological closing is then performed to get rid of the gaps between points (Fig. 3H). Then, the inertia matrix of the plain ellipse is computed and yields a major ( $\lambda_{maj}$ ) and minor axis ( $\lambda_{min}$ ). Back in the real space, the ellipse axes  $L_{maj} = \frac{2m}{\lambda_{min}}$  and  $L_{min} = \frac{2m}{\lambda_{maj}}$  define anisotropy. Again, the angles of eigenvectors,  $\theta$  and  $\theta + \pi/2$ , are the same in Fourier and real spaces. Note that here  $L_{min}$  and  $L_{maj}$  have no meaning in term of absolute cell size, as they are entirely dependent on the threshold parameter. However, they reflect the pattern anisotropy, as we will now discuss.

There are several families of acceptable definitions of internal strain [25]. Among them, one contains an infinity of acceptable definitions that are functions of  $L_{maj}, L_{min}$  [26]. We choose the “true” strain that was first introduced in the engineering field to describe large deformations [27]. Using the true strain formalism the anisotropic part of the cell strain is defined as a matrix with the same eigenvectors as the FT and with eigenvalues  $\pm \frac{1}{2} \log \frac{L_{maj}}{L_{min}}$  (see Appendix A). The absolute value of this amplitude (or its linearized approximations, if the strain is small, see Appendix A) is used as a measure of anisotropy that we call  $A$ , and that we represent as a bar in the direction  $\theta$  (Fig. 3I). The results are sensitive to the percentile of pixels kept for thresholding. However, a reasonable range of values allows to extract correct anisotropies (Fig. 8).

Altogether, the parameters to adjust for both methods are: window size and overlap, time average, Gaussian blur size, low cut-off for spatial frequencies; in addition, for FT ellipse ring fit: number of fit points; and for FT inertia matrix: percentile for thresholding, dilation-erosion size. The code is freely available on demand. It is user friendly and optimised to reduce the time it takes to manually adjust the parameters, typically 5 minutes at the beginning and 1 minute when the user is trained. Once these parameters are adjusted for a first image, they can be re-used for all similar images of the same series.

### III. RESULTS

#### A. Precision on cell size determination

To test the precision on cell size determination, we first test it on a set of artificial cellular patterns. Each image is created on a square of side  $L_{pix}$  pixels by sequentially placing  $N$  seeds at random points, with a minimum distance between them. Their Voronoi diagram is created, and the cell-cell junctions are thickened to reach a prescribed packing fraction (Fig. 4A). We measure the number of pixels per cell and the average cell size on the pattern. We then apply our pipeline and compute its error in cell size determination. This test is repeated on a series of 10 images with the same parameters (minimum distance between seeds, and packing fraction). Then the parameters are varied to generate a set of 600 different series.

Since we measure the cell size  $L$  from a peak in the FT, we expect the peak position in Fourier space to be around  $1/L$ . The precision in peak position determination is of order of one pixel in Fourier space, ie:  $\frac{1}{L\sqrt{N}}$ . The relative error on  $L$  is thus of order  $N^{-1/2}$ , independently of the number of pixels per cells  $N_{pix}$ . This is consistent with the results of our tests, where the value of  $N_{pix}$  has no effect as soon as it is larger than 20 (Fig. 4B) and the value of  $N$  is of order of  $0.83 N^{-1/2}$  (Fig. 4B,C). We thus recommend to select the window size in order to reach the requested resolution in size. Note that it would be possible to increase the resolution by padding the image - adding zeros around the picture - to decrease the pixel size in Fourier space.

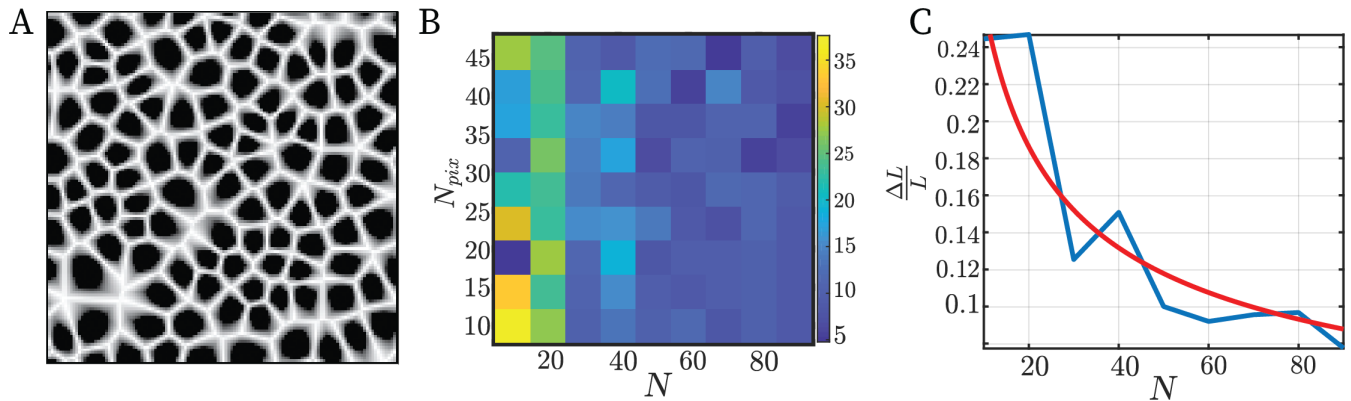


FIG. 4. Precision on cell size determination. *A*: Example of an artificial cellular pattern. Window size 128 pixels, at least 8 pixels between seeds, packing fraction 0.5,  $N = 80$  cells,  $N_{pix} = 158$  pixels per cell in average. *B*: Relative error on the cell size:  $\frac{\Delta L}{L}$ , where  $L$  is the average radius of the cells in the image vs number  $N$  of cells in the image and average number  $N_{pix}$  of pixels per cells. Data from 1260 images (126 series of 10 repeats). Each square is an average with a minimum of 10 images. *C*: Blue: error vs  $N$  for all images, ie: averaged on  $N_{pix}$ . Red: best fit by a  $N^{-1/2}$  law, prefactor 0.83.

## B. Cell size and anisotropy determination

To verify the cell size and anisotropy determination methods, we apply them on an image (Fig. 3A) whose quality is state of the art. Its segmentation (Fig. 1A) has been validated with an error rate lower than  $10^{-4}$  [10]. The study links tissue-level morphogenetic changes with cell-level processes such as cell shape changes, cell neighbour changes, divisions and apoptoses. The whole study involves movies of 300 images each, repeated several times for both wild-type and mutant conditions, thus implying the segmentation of tens of millions of cell contours. The FT calculation has been performed on a OSX with an Intel Core i7 processor at 2.2 GHz clock frequency. It takes about 60 minutes for the computation of the anisotropy part alone with the inertia matrix method, about 40 seconds for the computation of the size alone.

The cell anisotropy measurements using both the FT ellipse ring fit and the FT inertia matrix methods correlate with the segmentation measurements, qualitatively (Fig. 5A,B) and quantitatively (Fig. 5C,D) in amplitude and orientation. Both methods perform well in amplitude. As expected, the anisotropy orientation measurement is better when the anisotropy amplitude is larger; at small anisotropies the FT ellipse ring fit performs better than the FT inertia matrix.

The cell size measurements using the FT ellipse ring fit correlates well with the segmentation measurements, qualitatively (Fig. 5E,F) and quantitatively (Fig. 5G).

## C. Measurements on large dataset

We now test the FT analysis on a case where the cell number is particularly large. Data, kindly provided by C.J. Weijer, come from chicken morphogenesis, more precisely from a study of cell flows during primitive streak formation, estimating the relative contributions of cell shape changes and cell neighbour rearrangements [28]. Each image contains hundreds of thousands of cells (Fig. 6A). Altogether, taking into account wild-type and mutant conditions, hundreds of movies have been acquired, each with hundreds of images, resulting in several billion cells. The image quality and contrast are good enough for segmentation, but the cell number is too large and segmentation has been performed only on a subset of images.

Most boxes display clearly isotropic cell shapes (Fig. 6B), as quantitatively confirmed by their cell strain deviator (Fig. 6C). However, some boxes contain cells clearly displaying some shape anisotropy (Fig. 6D), as again quantitatively confirmed (Fig. 6E). These anisotropic cells are all located in a band, perpendicular to the anterioposterior (AP) axis, the so-called sickle region undergoing an extension. The question asked here is the width of the extended region. This does not require segmentation, and FT analysis seems appropriate.

Taking advantage of the expected band structure, we average the FT spectrum (Fig. 6F) over boxes in a rectangle perpendicular to the AP axis, strongly improving the signal to noise ratio (Fig. 6G): the ellipse ring becomes visible. We have the choice between both methods and choose here the FT inertia matrix, more robust than the FT ellipse ring fit to variations in image quality and contrast. By thresholding, calculating the inertia matrix and diagonalizing it,

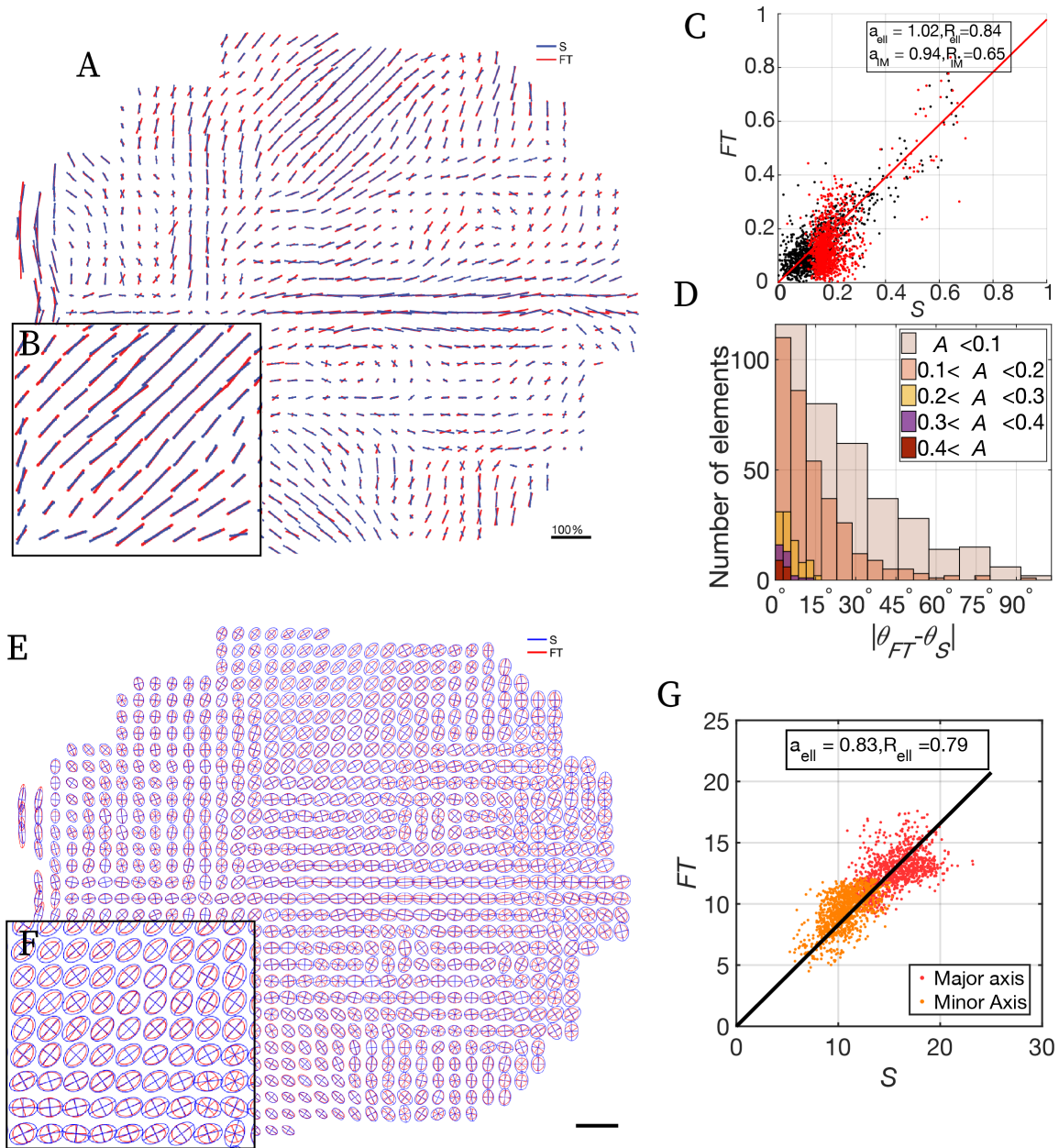


FIG. 5. Test of cell anisotropy and size measurements. (A) Map of cell anisotropies on the image in Fig. 1A. There are 1221 boxes of  $128 \times 128$  pixels with a 50% overlap. Blue bars: from segmentation, data of Fig. 1A. Red bars: from FT analysis computed with the inertia matrix. (B) Close up to a region of (A). (C) Measurements using FT ellipse fit ring (black) and FT inertia matrix (red) vs measurements using segmentation. Each point corresponds to a box. The slopes of the fit is 0.98 ( $R = 0.84$ ) for FT ellipse fit ring and 1.07 ( $R = 0.65$ ) for FT inertia matrix. (D) Histogram of the difference between angles from FT with the inertia matrix method, and from segmentation. The color codes for the cell strain deviator amplitude  $A$ . (E) Map of cell ellipses, representing cell sizes and anisotropies. Blue ellipse: from segmentation, data of Fig. 1A. Red ellipses: ellipses in real space, from FT analysis with the ellipse fit method. Scale bar is  $50 \mu\text{m}$ . (F) Close up to a region of (E). (G) Measurements using FT ellipse fit vs measurements using segmentation. Each point corresponds to a box; the slope of the fit is 1.18 ( $R = 0.79$ ).

we measure the anisotropy of the average FT (not the average of FT anisotropy). The calculation has been performed on a OSX with an Intel Core i7 processor at 2.2 GHz clock frequency. It takes 3 minutes for the computation of the anisotropy part alone with the inertia matrix method.

The FT clearly evidences the existence, position and width of the band, in good qualitative agreement with the segmentation (Fig. 6H). Quantitatively, the FT estimates the band full width at half maximum to  $446 \mu\text{m}$ , compared

with  $620\mu\text{m}$  using segmentation.

As a by product, FT provides the whole profile of anisotropy along the x axis, again in good qualitative agreement with the segmentation. Quantitatively, for boxes with anisotropy at least equal to 0.08, the agreement between FT and segmentation results is very good (Fig. 6I).

#### IV. CONCLUSION

In summary, we propose a Fourier Transform based analysis pipeline to measure the coarse grained field of pattern anisotropies and when the quality of the images is sufficient, to coarse grained sizes. It applies for instance to fixed or live, fluorescent and phase contrast images of epithelial tissues. The pipeline yields access to the cell strain deviator with the FT inertia matrix and returns a mechanically relevant measurement of cell anisotropy. Also when the image quality is sufficient, it can yield access to cell sizes with the FT ellipse ring fit of the spectrum.

After a user-friendly manual tuning of a few parameters, it can automatically handle tens of thousands of cells per second. We successfully validated it against segmentation based measurements. It is robust against defaults in image contrast, heterogeneities in cell sizes and orientations. It is adequate to improve the signal to noise ratio using space, time and/or ensemble averages; the latter are averages over samples and do not deteriorate the time or space resolution.

In a companion paper [29], we have used this principle to quantify the cell strain deviator on phase contrast images of a flow of Madin Darbey Canine Kidney cells around an obstacle. Extensions of applications could include ordered tissues, non-living cellular materials such as liquid foams, real-time analysis of live movies, tri-dimensional tissues.

#### ACKNOWLEDGMENTS

We warmly thank C.J. Weijer for chicken embryo data for providing images and for critical reading of the manuscript. We also thank F. Bosveld, S. Rigaud and Y. Bellaïche for their role in acquiring *Drosophila* pupa data.

- 
- [1] C.-P. Heisenberg and Y. Bellaïche, *Cell* **153**, 948 (2013).
  - [2] J. A. Zallen and R. Zallen, *J. Phys. Condens. Matter* **16**, 5073 (2004).
  - [3] A.-K. Classen, K. I. Anderson, E. Marois, and S. Eaton, *Dev. Cell* **9**, 805 (2005).
  - [4] T. Hayashi and R. W. Carthew, *Nature* **431**, 647 (2004).
  - [5] J. Käfer, T. Hayashi, A. F. M. Marée, R. W. Carthew, and F. Graner, *Proc. Natl. Acad. Sci. U. S. A.* **104**, 18549 (2007).
  - [6] S. Hilgenfeldt, S. Erisken, and R. W. Carthew, *Proc. Natl. Acad. Sci. U. S. A.* **105**, 907 (2008).
  - [7] R. Farhadifar, J.-C. Röper, B. Aigouy, S. Eaton, and F. Jülicher, *Curr. Biol.* **17**, 2095 (2007).
  - [8] M. Rauzi, P. Verant, T. Lecuit, and P.-F. Lenne, *Nat. Cell Biol.* **10**, 1401 (2008).
  - [9] G. B. Blanchard, A. J. Kabla, N. L. Schultz, L. C. Butler, B. Sanson, N. Gorfinkiel, L. Mahadevan, and R. J. Adams, *Nat. Methods* **6**, 458 (2009).
  - [10] B. Guirao, S. U. Rigaud, F. Bosveld, A. Bailles, J. López-Gay, S. Ishihara, K. Sugimura, F. Graner, and Y. Bellaïche, *Elife* **4**, e08519 (2015).
  - [11] R. Etournay, M. Merkel, M. Popović, H. Brandl, N. A. Dye, B. Aigouy, G. Salbreux, S. Eaton, and F. Jülicher, *Elife* **5** (2016), 10.7554/eLife.14334.
  - [12] E. Faure, T. Savy, B. Rizzi, C. Melani, O. Stašová, D. Fabrèges, R. Špir, M. Hammons, R. Čúnderlík, G. Recher, B. Lombardot, L. Duloquin, I. Colin, J. Kollár, S. Desnoullez, P. Affaticati, B. Maury, A. Boyreau, J.-Y. Nief, P. Calvat, P. Vernier, M. Frain, G. Lutfalla, Y. Kergosien, P. Suret, M. Remešková, R. Doursat, A. Sarti, K. Mikula, N. Peyriéras, and P. Bourguin, *Nat. Commun.* **7**, 8674 (2016).
  - [13] K. Sherrard, F. Robin, P. Lemaire, and E. Munro, *Curr. Biol.* **20**, 1499 (2010).
  - [14] M.-D.-C. Diaz-de-la Loza, R. P. Ray, P. S. Ganguly, S. Alt, J. R. Davis, A. Hoppe, N. Tapon, G. Salbreux, and B. J. Thompson, *Dev. Cell* **46**, 23 (2018).
  - [15] D. Heller, A. Hoppe, S. Restrepo, L. Gatti, A. L. Tournier, N. Tapon, K. Basler, and Y. Mao, *Dev. Cell* **36**, 103 (2016).
  - [16] S. Ishihara, P. Marq, and K. Sugimura, *Phys. Rev. E* **96**, 022418 (2017).
  - [17] F. Graner, B. Dollet, C. Raufaste, and P. Marmottant, *Eur. Phys. J. E* **25**, 349 (2008).
  - [18] R. O. Duda and P. E. Hart, *Commun. ACM* **15**, 11 (1972).
  - [19] S. J. Streichan, M. F. Lefebvre, N. Noll, E. F. Wieschaus, and B. I. Shraiman, *Elife* **7** (2018), 10.7554/eLife.27454.
  - [20] R. Lehoucq, J. Weiss, B. Dubrulle, A. Amon, A. Le Bouil, J. Crassous, D. Amitrano, and F. Graner, *Front. Phys.* **2**, 84 (2015).
  - [21] A. Bruns, *J. Neurosci. Methods* **137**, 321 (2004).
  - [22] A. Bruns, *J. Neurosci. Methods* **143**, 237 (2005).

- [23] F. Bosveld, I. Bonnet, B. Guirao, S. Tlili, Z. Wang, A. Petitalot, R. Marchand, P.-L. Bardet, P. Marcq, F. Graner, and Y. Bellaïche, *Science* (80-. ). **336**, 724 LP (2012).
- [24] L. Moisan, *J. Math. Imaging Vis.* **39**, 161 (2011).
- [25] K. Bagi, *Int. J. Solids Struct.* **43**, 3166 (2006).
- [26] K. Farahani and R. Naghdabadi, *Int. J. Solids Struct.* **37**, 5247 (2000).
- [27] H. Hencky, *J. Rheol. (N. Y. N. Y.)*. **2**, 169 (1931).
- [28] E. Rozbicki, M. Chuai, A. I. Karjalainen, F. Song, H. M. Sang, R. Martin, H.-J. Knölker, M. P. MacDonald, and C. J. Weijer, *Nat. Cell Biol.* **17**, 397 (2015).
- [29] S.Tlili, C. Gay, B. Ladoux, F. Graner, and H. Delanoë-Ayari, (2018), arXiv:1811.05001.
- [30] R. I. Tanner and E. Tanner, *E. Rheol Acta* , 42 (2003).

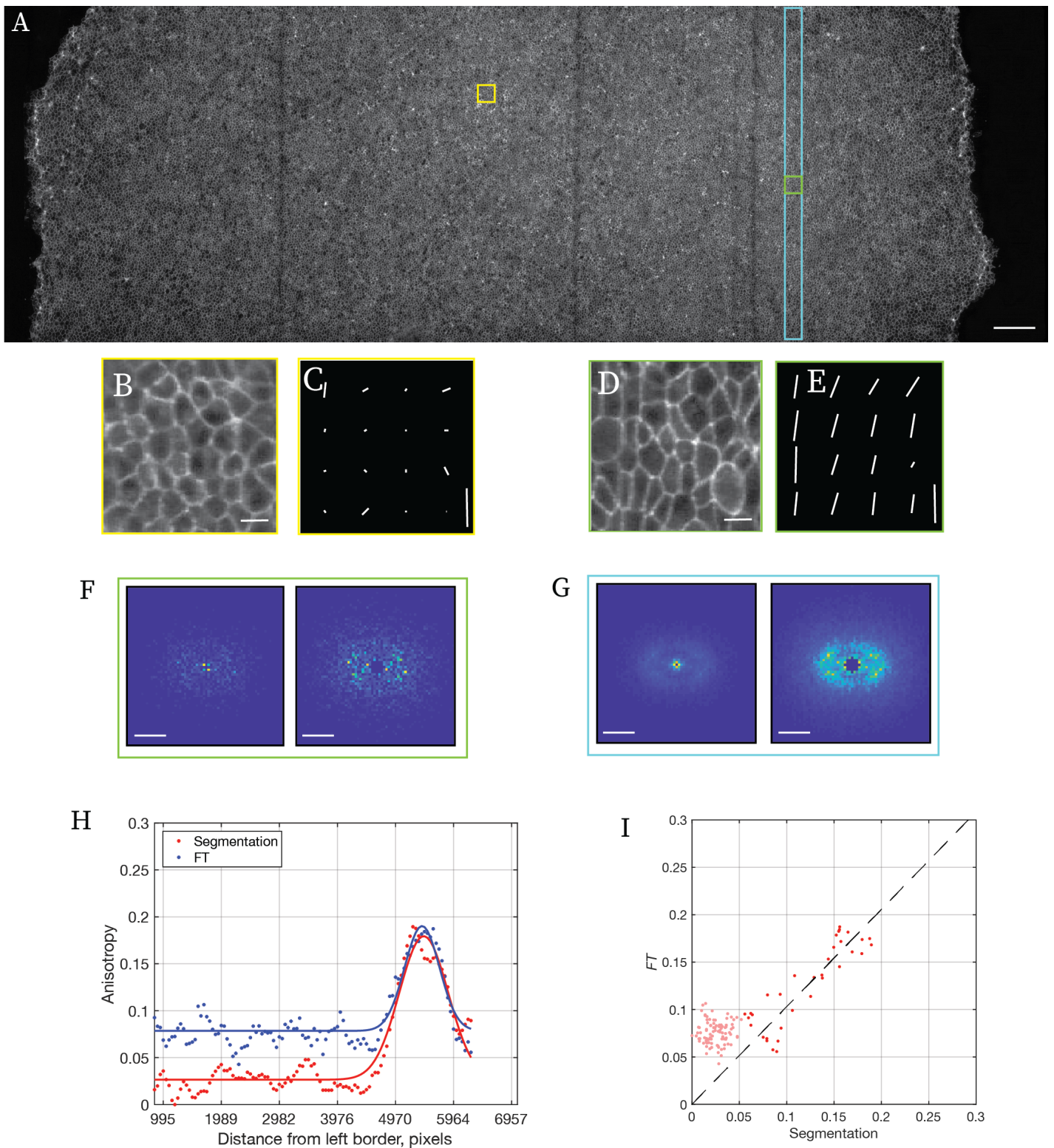


FIG. 6. Massive cell anisotropy measurements. (A) Light sheet microscopy image of chicken embryo at cellular resolution [28]. Scale bar is  $200 \mu\text{m}$ . The field of view contains around 100 000 cells. Anterioposterior (AP) axis is horizontal, with anterior on the left, posterior on the right. The two square boxes are  $200 \times 200$  pixels ( $\sim 100$  cells). (B, C) Close up of yellow box in A, and corresponding cell strain deviator measured by FT inertia matrix. (D, E) Same as B, C for green box in A, in the sickle region. For (B, D) scale bar is  $20 \mu\text{m}$ . For (C, E) scale bar is 10 % elongation. (F) Left: raw Fourier spectrum of the green box in A. Right: Same after removing small spatial frequencies and adapting the color scale. (G) Same as F, averaged over the whole region in the blue rectangular frame in A, perpendicular to the AP axis. Scale bar is  $10^{-1} \mu\text{m}^{-1}$ . (H) Anisotropy vs position along the AP axis. Averages are performed perpendicularly to the AP axis, as in G, and the anisotropy calculated after averaging. Red: measurements using segmentation. Blue: Measurements using FT inertia matrix. Gaussian fits give a width at half height of  $620 \mu\text{m}$  for the segmentation and  $446 \mu\text{m}$  for the FT. (I) Measurements using FT inertia matrix vs measurements using segmentation; pink dots are regions of small anisotropies. Same data as in H. Dashed line: linear fit, slope 1.05 ( $R = 0.91$ ), performed on data points with anisotropy at least equal to 0.08.

### Appendix A: Matrices used in the text

We introduce here three types of  $2 \times 2$  matrices, also called rank-2 tensors: the inertia matrix, the FT inertia matrix and the cell strain.

The inertia matrix of a binarized pattern is defined by:

$$I = \begin{pmatrix} \langle xx \rangle & \langle xy \rangle \\ \langle xy \rangle & \langle yy \rangle \end{pmatrix} \quad (\text{A1})$$

Here  $x$  and  $y$  are coordinates with origin at the pattern barycenter,  $\langle x \rangle = \langle y \rangle = 0$ . The brackets indicate an average over the coordinates within the pattern (if the pattern was in grey levels instead of being binarized, the average would be weighted by the grey levels). The four terms which appear in  $I$  are the coordinate covariances.

The FT inertia matrix has the same definition, Eq. (A1), but it operates in the Fourier space. Here  $x$  and  $y$  are coordinates in the space of spatial frequencies, again with origin at the pattern barycenter,  $\langle x \rangle = \langle y \rangle = 0$ .

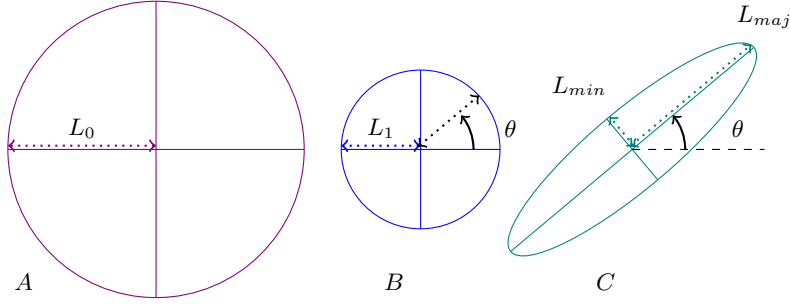


FIG. 7. Strain: isotropic and anisotropic contributions. Under a purely isotropic deformation, or growth (positive or negative), a disk of radius  $L_0$  (A) transforms into a disk of radius  $L_1$  (B). Under a purely anisotropic deformation, or convergence-extension, a disk of radius  $L_1$  (B) transforms into an ellipse of major axis  $L_{maj}$ , in direction  $\theta$ , and minor axis  $L_{min}$ , in perpendicular direction, with area conservation expressed by  $L_{maj}L_{min} = L_1^2$  (C).

The cell strain has an isotropic and anisotropic contributions (Fig. 7)

$$\varepsilon_c = \frac{1}{2} \text{tr}(\varepsilon_c) \mathcal{I}_2 + \varepsilon_c^{dev} \quad (\text{A2})$$

where  $\mathcal{I}_2$  is the identity matrix in 2 dimensions.

Consider a circle of radius  $\ell$  (Fig. 7) and apply a small variation of its length  $d\ell$ . Its relative extension is  $d\ell/\ell = d(\log \ell)$ . Integrating this infinitesimal extension between the initial and final states yields the expression for strain [30] which for the isotropic part writes (Fig. 7A,B):

$$\frac{1}{2} \text{Tr}(\varepsilon_c) \mathcal{I}_2 = \frac{\log(L_1/L_0)}{2} \begin{pmatrix} 1 & 0 \\ 0 & 1 \end{pmatrix} \quad (\text{A3})$$

and for the anisotropic part, and after diagonalisation along axes of directions  $\theta$  and  $\theta + \pi/2$  (Fig. 7B,C):

$$\varepsilon_c^{dev} = \begin{pmatrix} \log\left(\frac{L_{maj}}{L_1}\right) & 0 \\ 0 & \log\left(\frac{L_{min}}{L_1}\right) \end{pmatrix} = \begin{pmatrix} \frac{\log(L_{maj}/L_{min})}{2} & 0 \\ 0 & -\frac{\log(L_{maj}/L_{min})}{2} \end{pmatrix} \quad (\text{A4})$$

where  $L_1 = \sqrt{L_{maj}L_{min}}$ . The cell strain deviator amplitude is  $\frac{1}{2} \log \frac{L_{maj}}{L_{min}}$ , and the cell strain deviator orientation is  $\theta$ . The cell strain deviator can be inferred from the pattern anisotropy, without requiring any information about the current cell size  $L_1$  or its rest state value  $L_0$ ; the above derivation only assumes that the rest state is isotropic. Note that this definition of the strain is called the “true” strain, or Hencky strain [27]. When the cell strain deviator amplitude is much smaller than one, one can alternatively use any approximation equivalent at first order, such as  $\frac{1}{2} \left( \frac{L_{maj}}{L_{min}} - 1 \right)$ , for instance when using the linear approximation to the true strain, or  $\frac{1}{4} \left( \frac{L_{maj}^2}{L_{min}^2} - 1 \right)$ , when using quadratic tensors attached to the matter (inertia or texture tensor) [17].

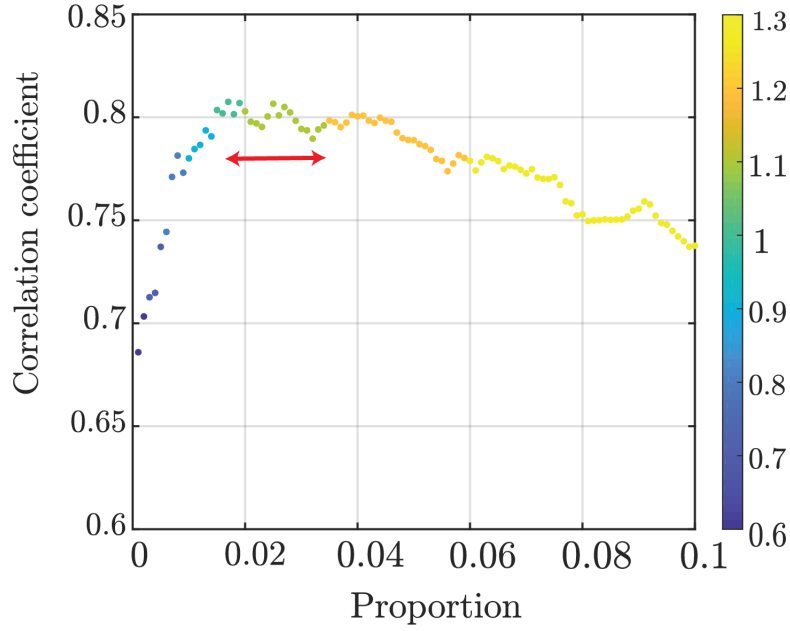


FIG. 8. Evolution of the correlation coefficient between the anisotropy amplitudes extracted from FT and from segmentation on the *Drosophila* pupa dataset with the proportion parameter. The colorbar represents the value of the slopes of the correlations, ie: a slope one signifies that FT and segmentation yield the same values of anisotropies, a slope 1.2 signifies that the values extracted from FT are 1.2 times larger. The proportion reaches an optimal criteria around 0.02% where the correlation coefficient is at its highest and the value of the slope is 1. There is a significant range of acceptable values, as shown by the arrow, easily accessible using the software interface.

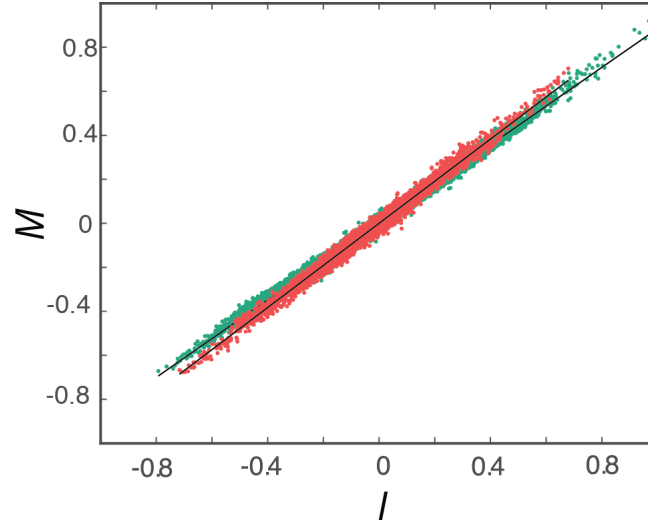


FIG. 9. Data presented here are from the same dataset as Fig.1. Diagonal component (green) and off-diagonal component (red) of the texture tensor  $M$  as defined in [17] versus the corresponding anisotropic (diagonal and off-diagonal) component of the inertia matrix  $I$ , representing cell shape anisotropy. Correlations coefficients are respectively 0.99 and 0.98, slopes are respectively 0.88, 0.96. Tensors built with data from [10], here plotted after adimensionalisation by the isotropic part of the respective tensor. To compute each of the 14112 points, tensors of individual cells are computed before being averaged in Eulerian grids of  $40 \times 40 \mu\text{m}^2$  with 50% overlap. Then a sliding average is performed on 2 h (24 frames) of time with a one hour overlap. Boxes at the pattern boundary which are filled at less than 30% by cells are excluded from the fit.